# New routes to food gels and glasses

**8 AUTHORS**, INCLUDING:

Thomas Gibaud
Ecole normale supérieure de…

**22** PUBLICATIONS **410** CITATIONS

Jan Skov Pedersen
Aarhus University

**363** PUBLICATIONS **10,961** CITATIONS

# New routes to food gels and glasses

Thomas Gibaud,[ab] Najet Mahmoudi,[c] Julian Oberdisse,[d]
Peter Lindner,[e] Jan Skov Pedersen,[f] Cristiano L. P. Oliveira,†[f]
Anna Stradner[g] and Peter Schurtenberger*[g]

We describe the possibility to create solid-like protein samples whose structural and mechanical properties can be varied and tailored over an extremely large range in a very controlled way through an arrested spinodal decomposition process. We use aqueous lysozyme solutions as a model globular protein system. A combination of video microscopy, small-angle neutron and X-ray scattering and reverse Monte Carlo modeling is used to characterize the structure of the bicontinuous network with two coexisting phases of a dilute protein solution and a glassy or arrested dense protein backbone at all relevant length scales. Rheological measurements are then used to determine the complex mechanical response of these protein gels as a function of protein concentration and quench temperature. While in particular the origin of the dependence of the mechanical properties on quench depth and concentration is not well understood currently, it seems ultimately connected to the particular bicontinuous structure of the arrested spinodal network created by the interplay between the early stage of a spinodal decomposition and the position of the glass line. We then generalize this behavior and discuss how this could open up new routes to prepare gel-like food systems with adjustable structural and mechanical properties. We present results from a first feasibility study where we use a depletion interaction caused by the addition of small non-adsorbing polymers to suspensions of casein micelles in order to create food gels with tunable structural and mechanical properties through an arrested spinodal decomposition process.

## 1 Introduction

Gels and glasses play a very important role in today's food science and technology.[1] Typical examples of food gels are yoghurt or cheese, where soft solid-like food materials are created through the irreversible aggregation of casein micelles, a prime representative of food colloids. Currently, the majority of food gels are based on sometimes quite elaborate and energy-intensive processing steps such as heat or

[a]Brandeis University, 415 South Street, Waltham, MA 02453, USA

[b]Université de Lyon, Laboratoire de Physique, École Normale Supérieure de Lyon, CNRS UMR 5672 - 46 Alle d'Italie, 69364 Lyon cedex 07, France

[c]Sector of Biological and Soft Systems, Cavendish Laboratory, University of Cambridge, J.J. Thomson Avenue, CB3 0HE Cambridge, UK

[d]Laboratoire Charles Coulomb Université Montpellier 2/CNRS UMR 5221, F-34095 Montpellier, France

[e]Institut Laue-Langevin, B.P. 156, Grenoble, France

[f]Department of Chemistry, University of Aarhus, Langelandsgade 140, Aarhus C, Denmark

[g]Lund University, Division of Physical Chemistry, Lund, Sweden

† Current address: Instituto de F'sica, Universidade de S'o Paulo, Caixa Postal 66318, 05314-970 S'o Paulo, Brasil

pressure treatments. It is thus quite obvious that food science and engineering could <span style="color:blue">View Article Online</span> enormously profit from parallel developments in colloid science, where fluid–solid transitions such as dynamical arrest, jamming or gelation frequently encountered in colloidal suspensions have been at the center of experimental and theoretical activities during the last few years.

These investigations of dynamical arrest in colloidal suspensions have been mainly triggered by attempts to make and exploit analogies between the resulting phase or state diagrams of colloidal suspensions and atomic and molecular systems. Numerous studies have demonstrated the presence of solid-like structures such as particle gels or colloidal glasses under conditions where either repulsive or attractive interactions dominate.[2–5] Particularly interesting are also systems where mixed potentials, *i.e.* a combination of a short range attraction and a large range soft repulsion, exist.[2,6] Our current state of understanding of the phenomenon of dynamical arrest in systems with mixed potentials as a function of the strength of the attractive part and of the range of the soft repulsive part of the interparticle interaction potential is schematically summarized in Fig. 1.
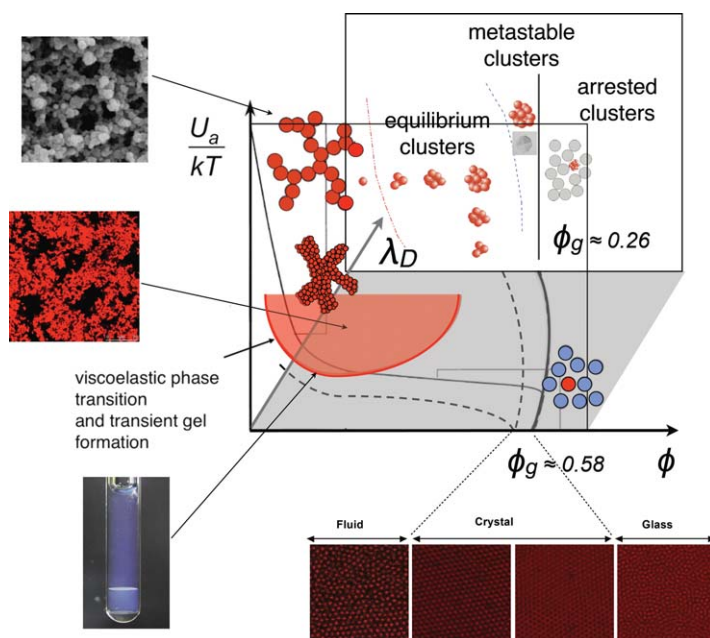


**Fig. 1** Schematic state diagram of colloidal particles with mixed interaction potentials consisting of a short range attraction of strength $U_a$ and a screened Coulomb repulsion with screening length $\lambda_D$. Shown are the freezing line (dashed line) as well as the arrest line (solid line) as a function of volume fraction $\phi$, $U_a$ and $\lambda_D$. Three cases are particularly highlighted: (1) short range attractive particles, where a metastable liquid–liquid phase separation occurs in addition to the commonly found liquid, crystalline and glassy or gel states; (2) purely repulsive systems; and (3) particles with mixed potentials where the range of the soft repulsion is significantly larger than the attraction, and where one also finds an equilibrium cluster phase and a cluster glass. Also shown are several examples from the different regions of this state diagram. The scanning electron microscopy (SEM) picture shown in the upper left part illustrates the formation of particle gels for strong attraction (casein micelles in yoghurt formation). Also shown is a confocal laser scanning microscopy (CLSM) picture of a particle gel formed by arrested spinodal decomposition (casein micelles with added polymer, left middle), a photograph of a protein solution that has undergone liquid–liquid phase separation (lower left corner), and a sequence of CLSM pictures of colloidal suspensions with increasing $\phi$ that shows fluid, crystalline and glassy states (adapted after ref. 1).

For ideal hard sphere particles, we observe a transition from a liquid to a disordered solid phase, a glass, at volume fractions of approximately $\phi \approx 0.58$.[7] If a weak and short-ranged attraction is now turned on, this leads to the astonishing observation of a melting of the glass, followed by a so-called re-entrant glass or solid formation at even stronger attractions.[3,8,9] In the other extreme case of very strong interparticle attraction, we reach the regime of so-called irreversible aggregation where one observes the formation of soft fractal gels already at very low volume fractions.[9,10] At intermediate strength of the attraction, the situation is even more complicated due to the fact that phase separation into a dilute (gas-like) and a concentrated (liquid-like) suspension can occur. The position of the corresponding coexistence curve can then intersect with the arrest or gel line, and the phase separation can subsequently lead to the formation of a long-lived interaction network of particles, if the attractive interactions between them are strong enough.[11]

When now adding a screened Coulomb repulsion, we see a significant move of the freezing line to lower values of $\phi$, accompanied by a similar evolution of the glass line. In the extreme case of fully de-ionized colloidal suspensions, crystallization can occur at volume fractions as low as $10^{-3}$ or lower.[12,13] When combined with a short range attraction, new states appear, the metastable liquid–liquid phase separation is suppressed and we observe the formation of (transient) equilibrium clusters.[14] The ability of colloidal particles to form equilibrium cluster phases under conditions where the particles interact *via* such mixed potentials is well documented.[6] In this class of systems, the short range attraction drives cluster formation, whereas the increasing long-range repulsion due to the accumulating charge of the clusters limits their size. Cluster phases have been demonstrated to exist in a large range of colloidal systems[15–19] and protein solutions.[14,20–26] Particularly interesting in this context is the fact that such protein clusters were found to undergo an arrest transition from a cluster fluid to a cluster glass that occurs at a significantly lower volume fraction $\phi_g \approx 0.26$ when compared to the hard sphere glass at $\phi_g \approx 0.58$.[6]

The schematic state diagram shown in Fig.1 is however not only relevant for colloidal model systems, but has already been used to rationalize the behavior of food systems and provide guidelines for creating materials.[1] Food colloids such as casein micelles have been shown to closely follow theoretical descriptions originally developed for colloidal model systems, and the analogy between the structure of dense colloid gels used in sol–gel ceramics production and casein particle gels produced in yoghurt formation has for example allowed to understand and model this important food process quantitatively.

An important technological challenge in food technology is to optimize the mechanical properties of food gels and simplify the processing by controlling interparticle interactions between food colloids such as proteins. In an ideal case, this would then allow for creating food gels with tailored structural and mechanical properties through controlled self-assembly without invoking costly processing steps such as heat or pressure treatment. It is in this context that the widely differing solid-like states encountered with colloids offer interesting possibilities. In particular the existence of an arrest line that extends into the spinodal region for colloids with short range attractions appears very attractive. It has already been reported previously that quenching such a system deeply enough into the spinodal such that the equilibrium concentration of the dense phase would be located in the arrested region of the state diagram will lead to solid-like materials where the bicontinuous structure resembles those found during classical spinodal decomposition, with a correlation length mainly determined by the quench depth.[27] It seems quite conceivable that this could offer a mechanism that would allow us to create food gels with controllable mechanical and structural properties.

However, while the phenomenon of an arrested spinodal decomposition as a possible mechanism for gelation in attractive colloidal suspensions appears to be generally accepted, there exist contradicting findings as to the location of the arrest line.[11,28] The presence of an arrested spinodal decomposition has for example been

demonstrated for concentrated solutions of the model protein lysozyme which is known to exhibit a phase diagram that closely matches the predictions for colloids with short-ranged attractions.[11] Here the mechanism underlying the liquid–solid transition encountered when quenching a protein sample deeply below the coexistence curve for liquid–liquid phase separation has been interpreted based on a state diagram as shown in Fig.1. It has been proposed that arrest occurs because the spinodal decomposition process leads to a bicontinuous structure which gets "pinned" into a rigid self-supporting network when the concentration of the high density regions crosses the arrest line and subsequently undergo dynamical arrest. This scenario has been supported by several studies using lysozyme,[11,27,29] it is however in sharp contrast to one of the central conclusions drawn in ref. 28, where a universal phase diagram for colloids with short-range attraction had been constructed that suggested that the gelation line coincides with the phase separation boundary in the Baxter model. These authors then concluded that the origin of dynamical arrest came from the dense phase undergoing an attractive glass transition at $\phi_g \approx 0.55$, and claimed that the attractive glass line would thus not extend into the phase separation region but instead follow its high density boundary.

It is clear that the possibility to create solid-like food materials with tunable structural and mechanical properties through an arrested spinodal decomposition process will ultimately depend on which one of these scenarios is correct, as only the first scenario will lead to a large accessible range of mechanical properties. We thus further explore the nature of the arrested spinodal decomposition process and the resulting structures and their mechanical properties of lysozyme solutions as a model for food proteins. We then investigate whether the same structures can be generated for much larger particles such as casein micelles, now using depletion interaction from added non-adsorbing (bio)polymers to create the necessary short range attraction.

## 2  Materials and methods

We use hen egg white lysozyme (Fluka, L7651) dispersed in an aqueous buffer (20 mM Hepes, pH = 7.8) containing 0.5 M sodium chloride. Lysozyme is a monodisperse globular protein of a molecular mass of 14.4 kDa carrying a net charge of +8 electronic charges at pH = 7.8. Details of the sample preparation are given in ref. 11. Initially a suspension at $\phi \approx 0.22$ is prepared in pure buffer without added salt, and its pH is adjusted to 7.8 ± 0.1 with sodium hydroxide. Under these conditions the solution is stable and is used as stock. We then dilute it with a NaCl-containing buffer at pH = 7.8 to a final NaCl concentration of 0.5 M. Particular care is taken to avoid partial phase separation upon mixing by pre-heating both buffer and stock solution well above the coexistence curve for liquid–liquid phase separation. This procedure results in completely transparent samples at room temperature with volume fractions ranging from $\phi = 0.01$–0.18, where $\phi$ was obtained from the protein concentrations $c$ measured by UV absorption spectroscopy using $\phi = c/\rho$, where $\rho = 1.351 \ g/cm^3$ is the protein density. To prepare samples at even higher volume fractions up to $\phi \approx 0.34$, we take advantage of the ability of the system to phase separate into a protein-rich and protein-poor phase.

Temperature quenches to investigate samples undergoing an arrested spinodal decomposition were done as described in ref. 27: The cuvette (1 mm Hellma quartz cell or 1 mm capillary) used in the experiment was filled with a fresh lysozyme dispersion around 25 °C. The sample is then pre-quenched for a minute in an ethanol bath at the desired final temperature, $T_f$. It is then quickly transferred to the thermostated cuvette holder of the experiment, also at $T_f$. This procedure allows to obtain quench rates where we estimate the time for the sample to go from 25 °C to $T_f$ to be around 30 s.

The feasibility tests using casein micelles were made with casein micelles free from whey proteins and from lactose (Micellar Caseins, MPI-85MC) with an

This journal is © The Royal Society of Chemistry 2012

average hydrodynamic radius of $R_h = 100$ nm provided by the Hungarian Dairy Research Institute. As a flexible polymer for inducing depletion interactions we used poly(ethylene oxide) (PEO) from Polymer Source, Inc. It has a weight average molar mass, $M_w$, of 102 000 g mol$^{-1}$, a polydispersity index of 1.08 and a radius of gyration, $R_g$, of 15.86 nm, as stated by the manufacturer. Mixtures of casein micelles at a fixed volume fraction of 0.25 and PEO at various concentrations at neutral pH and an ionic strength of 100 mM NaCl were prepared from casein and PEO stock solutions using a minishaker (MS1 Minishaker, IKA) in plastic cuvettes. The ionic strength was adjusted using a concentrated NaCl solution. The casein micelles were labelled with Rhodamine B for confocal laser-scanning microscopy (CLSM) imaging.

The microstructure of casein micelles dispersed in PEO was captured using a Leica TCS SP5 confocal laser-scanning microscope (CLSM) operated with a 63× glycerol-immersion objective. A square pixel slice was taken (512 × 512) with image dimensions varying from 246 × 246 to 25 × 25 μm. Z-stacks were acquired until a depth of approximately 30–40 μm.

Small-angle neutron (SANS) and X-ray (SAXS) scattering experiments were performed on lysozyme samples that underwent an arrested spinodal decomposition process. SANS experiments were performed at the SANS I facility at the Swiss neutron source SINQ at the Paul Scherrer Institut, Switzerland, and at the instrument D11 at the Institute Laue Langevin in Grenoble, France. We used 1 mm Hellma quartz cells and a thermostatically regulated sample holder. Combinations of different wavelengths, sample-to-detector distances and collimation lengths were used to cover a $q$ range of 0.015 to 2 nm$^{-1}$. In the SANS experiments, the contrast, $K$, depends on the scattering length density of water, $\rho_W = -5.60 \times 10^{-7}$ Å$^{-2}$, the scattering length density of lysozyme, $\rho_L = 1.88 \times 10^{-6}$ Å$^{-2}$, the partial specific volume of lysozyme, $v = 0.74$ mL g$^{-1}$ and Avogadro's number, $N_A$. It is equal to $K = v^2(\rho_L - \rho_W)/N_A = 5.41\ 10^{-8}$ m$^2$ mol g$^{-2}$. SAXS experiments were carried out with a pinhole camera (NanoSTAR, Bruker AXS) employing a rotating anode (Cu K$_a$) X-ray source, a thermostatically regulated sample chamber and a two-dimensional gas detector. For the present experiments the sample to detector distance was 24 cm, providing a $q$ range of 0.2 to 10 nm$^{-1}$.[30]

We also measured the rheological properties of the arrested spinodal network with a stress-controlled rheometer (MCR300 from PaarPhysica) in a cone and plate geometry, using a solvent trap to minimize sample evaporation. In a typical experiment we loaded a sample in the rheometer at $T = 25\ °C$, i.e., well above the binodal line. $T$ was then lowered to the final temperature of the quench, $T_f$. Once the temperature in the rheometer reached $T_f$, the sample was left to rest for 300 s during which the structure stabilizes. This procedure enabled us to reach a reproducible steady state with negligible aging. Two types of tests were then carried out to characterize the viscoelastic properties of the arrested spinodal decomposition in the linear response regime: (i) frequency sweeps giving $G'$ and $G''$ as a function of the frequency $f$, and (ii) creep experiments which yield the compliance $J(t)$ as a response to a step stress. These two measurement protocols gave consistent results.

## 3  Results and discussion

### 3.1  Arrested spinodal decomposition in lysozyme solutions

The phase diagram of lysozyme at 0.5 M NaCl has been described in detail previously.[11,27,31] It shows all the characteristic features of colloids interacting via a short range attractive potential such as liquid–liquid phase separation that is metastable with respect to the liquid–solid (crystal) phase boundary. The location of the binodal is shown again in Fig. 2a. Samples quenched below the binodal into region I show macroscopic phase separation as demonstrated by the photograph in Fig. 2a. However, for quenches below the tie line at 15 °C the phase separation becomes
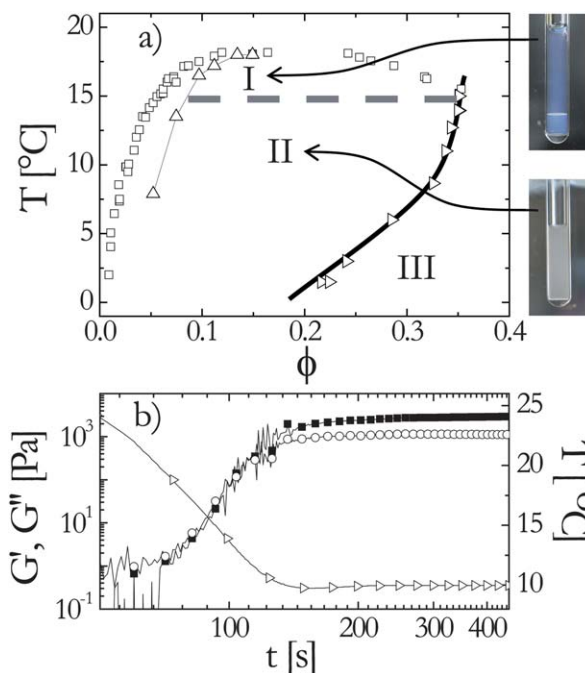
Fig. 2 a) State diagram of lysozyme. Liquid–liquid phase boundary (binodal, □), spinodal (△), glass line (▷), as determined in ref. 11, and tie line that separates complete phase separation from arrested spinodal decomposition (dashed line). Region I: phase separation. Region II: arrested spinodal decomposition. Region III: glass. b) Measurements of $G'$ (■) and $G''$ (○) at 1 Hz during a temperature quench from 25 °C to $T_f = 10$ °C (▷) at $\phi = 0.11$.

arrested.[11] This can be seen in Fig. 2b, where the evolution of the storage ($G'$) and loss ($G''$) moduli as a function of temperature $T$ are shown. As $T$ decreases from 25 °C to $T_f$, the sample first becomes turbid at the binodal line as a result of the spinodal decomposition (lower photograph in Fig. 2a). At $T \simeq 15$ °C, the sample then undergoes a fluid to solid transition. The bicontinuous appearance clearly visible in video microscopy no longer evolves, and the correlation length $\xi$ linked to the characteristic mesh size of the bicontinuous network gets pinned as described in ref. 27. The corresponding evolution of the storage ($G'$) and loss ($G''$) moduli with time measured at 1 Hz is shown in Fig. 2b, and we see that $G'$ increases above $G''$ at $T \simeq 15$ °C.

## 3.2 Structure of the arrested network from SANS and SAXS

It has previously been proposed that systems that have undergone an arrested spinodal decomposition have a bicontinuous structure with a protein-poor fluid and a dense glassy protein network as sketched in Fig. 1.[27] Estimates of the local volume fraction in the dense strands have been determined by centrifugation experiments, and the resulting concentrations correspond to the volume fraction of the "homogeneous" attractive glass at the arrest line within the spinodal region separating region II and III in Fig. 2a.[11] Previous characterizations of the network structure have mainly concentrated on revealing the bicontinuous network and its correlation length $\xi$.[27] However, no direct and quantitative characterization of the network structure at all relevant length scales has been reported so far. A major problem here are the extremely different length scales that characterize these samples, with a correlation length of the network $\xi \sim$ μm, while the local nearest neighbor distance

in the dense glassy branches must be of order protein diameter $\sigma = 2a \approx 3.4$ nm where $a$ is the protein radius.‡

In a next step we thus take a closer look at the local structure of the arrested spinodal network probed with SAXS and SANS. These are ideal techniques to reveal the internal structure on complementary length scales all the way to the single protein monomer. We aim at characterizing the interface between the gas-like and the glass-like phases and the local structure of the glass-like phase. The results from a corresponding combined SANS and SAXS study of the dependence of the network structure as a function of initial sample concentration and quench depth, *i.e.* final temperature $T_f$, are shown in Fig. 3 together with typical video micrographs of samples that underwent an arrested spinodal decomposition.

The micrographs for samples obtained at different quench depths shown in Fig. 3a indeed demonstrate that the arrested spinodal decomposition results in a bicontinuous network with decreasing mesh size, *i.e.* decreasing correlation length $\xi$. The SANS and SAXS data in Fig. 3b and c summarize the evolution of the intensity as a function of the final temperature $T_f$ after a quench at $\phi_0 = 0.148$ (Fig. 3b) and the evolution of the intensity as a function of the initial volume fraction, $\phi_0$, at 10 °C (Fig. 3c), respectively. At low $q$ we observe a Porod regime, $I \sim q^{-4}$, which confirms that the gel is indeed a bicontinuous network with a sharp interface between the dilute (gas-like) and the dense glass-like phases. As temperature decreases, the intensity in the Porod regime increases, reflecting an increase of the surface to volume ratio of the glassy backbone. One can deduce the surface to volume ratio from the Porod regime:

$$I_{\mathrm{Porod}}(q) = \frac{2\pi\Delta\rho^2}{q^4}\frac{S}{V} \qquad (1)$$

The excess scattering length density $\Delta\rho$ defines the contrast between the gas-like and the dense phases. The gas-like phase is characterized by its lysozyme volume fraction $\phi_1$ and the relative volume of the gas-like network branch $1 - h$, while the dense phase is characterized by its lysozyme volume fraction $\phi_2$ and the relative volume of the dense network branch, $h$, where $h$ is the relative height of the dense phase for a macroscopically separated sample as determined using centrifugation experiments (see ref. 11 for details). For SANS $\Delta\rho$ can be approximated by

$$\Delta\rho = [\rho_L\phi_2 + (1 - \phi_2)\rho_W] - [\rho_L\phi_1 + (1 - \phi_1)\rho_W] \qquad (2)$$

The results of the calculation of the surface to volume ratio $S/V$ using eqn (1) and 2 are tabulated in Tab. 1 together with an analysis of the correlation lengths $\xi$ from microscopy. We find that $S/V$ increases with decreasing temperature, which seems reasonable as the characteristic length $\xi$ decreases with decreasing temperature. For a given quench temperature, it also increases with decreasing concentration, which again agrees with the fact that both the local volume fractions $\phi_1$ and $\phi_2$ as well as the correlation length $\xi$ are independent of the initial concentration and depend on the final temperature only.

## 3.3 Local structure

At larger $q$ the intensity reflects the local organization of the dense phase, which depends on the local volume fraction but also on the interactions between the proteins. Given the fact that we expect the local structure to exhibit only weak variations as the system dynamically arrests when crossing the arrest line, we use liquid state theory to calculate the effective static structure factor $S(q)$ at length scales

‡ Note that these are average values, as lysozyme has an approximately ellipsoidal shape with two minor axes of about 3.3 nm and a major axis of about 5.5 nm diameter.
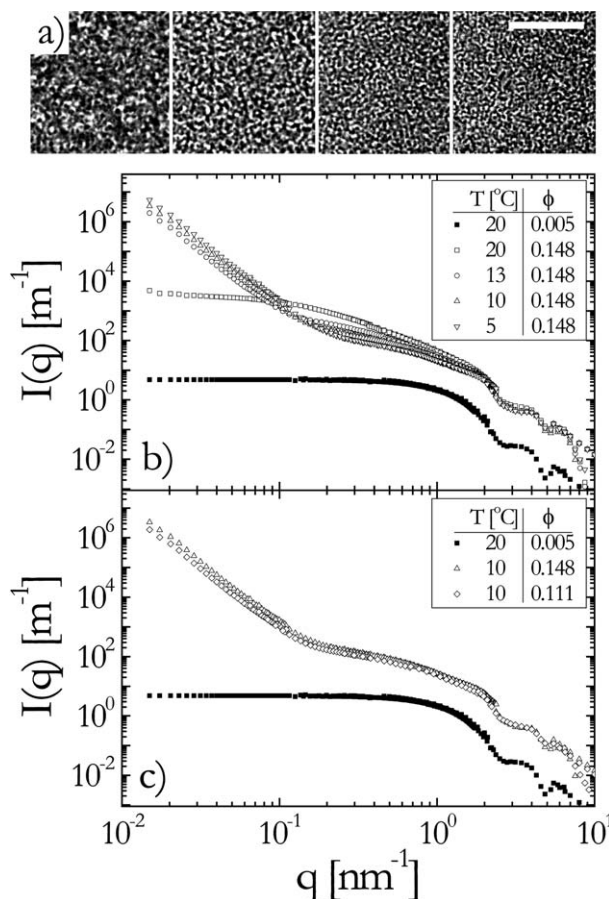
**Fig. 3** a) Micrographs showing arrested spinodal decomposition for a fast quench at (from left to right): $T_f = 15\ °C$, $T_f = 10\ °C$, $T_f = 5\ °C$, $T_f = 1\ °C$. The scale bar is 20 μm. b) SANS and SAXS results for a temperature series at constant concentration ($\phi = 0.148$): 20 ($\square$), 13 ($\bigcirc$), 10 ($\triangle$), 5 °C ($\triangledown$), and for a sample at low concentration (form factor, $\phi = 0.005$) at 20 °C ($\blacksquare$); and c) concentration series at constant $T_f = 10\ °C$: $\phi = 0.111$ ($\diamond$) and $\phi = 0.148$ ($\triangle$), as well as $\phi = 0.005$, at 20 °C ($\blacksquare$) as an effective form factor. Note that due to the different scattering contrast for SANS and SAXS, the SAXS data have been rescaled to the SANS data. Moreover, there is a slight mismatch in the overlap region due to the fact that for SAXS the electron density of the hydration shell is larger than that of bulk water, which results in a slightly larger effective radius of gyration for lysozyme in SAXS experiments than in SANS. $q = 1.5 \times 10^{-2}$–$2\ nm^{-1}$: SANS data. $q = 0.3$–$10\ nm^{-1}$: SAXS data.

comparable to the monomer diameter. The effective structure factor $S(q)$ is determined as the ratio between two measurements normalized with the particle concentrations:

$$S(c, \phi) = \frac{I(q, \phi)\phi_{\text{dilute}}}{\phi I(q, \phi_{\text{dilute}})} \tag{3}$$

where $I(q,\phi)$ is the intensity scattered by a solution of volume fraction $\phi$ and $I(q,\phi_{\text{dilute}})$ is the intensity of the dilute sample, $\phi_{\text{dilute}} = 0.005$, used as the effective form factor. Typical results for samples after an arrested spinodal decomposition are shown in Fig. 4.

We then compare the scattering results with model calculations where we use a square-well potential to approximate the protein–protein interactions. Here $S(q)$

**Table 1** Variation of $\phi_1$, $\phi_2$, $h$ (obtained from the centrifugation experiments[11]), $\xi$ (obtained from the microscopy experiments shown in Fig. 7) and $S/V$, the surface to volume ratio (extracted from the Porod regime) as a function of $T_f$ and $\phi_0$

| $T_f$ [°C] | 13 | 10 | 5 | 10 |
|---|---|---|---|---|
| $\phi_0$ | 0.148 | 0.148 | 0.148 | 0.111 |
| $\phi_1$ | 0.048 | 0.041 | 0.026 | 0.041 |
| $\phi_2$ | 0.344 | 0.329 | 0.270 | 0.329 |
| $h$ | 0.342 | 0.381 | 0.520 | 0.242 |
| $\xi$ [μm] | ~3.5 | ~2.5 | ~1.9 | ~2.5 |
| $S/V$ [nm$^{-1}$] | 76 | 186 | 331 | 327 |
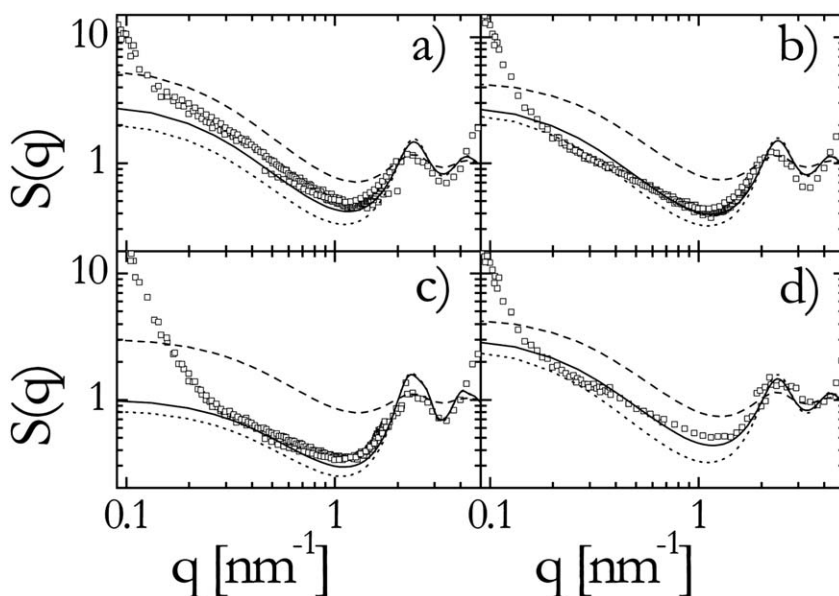


**Fig. 4** Effective structure factor of the arrested spinodal decomposition. Symbols are data from SAXS experiments, lines calculated structure factors for the dilute phase $S_1(q)$ (dashed line), the concentrated phase $S_2(q)$ (dotted line) and the total effective structure factor $S_{cal}(q)$ (solid line), respectively (see text for details). a) Quench at 13 °C with $\phi_0 = 0.148$. b) Quench at 10 °C with $\phi_0 = 0.148$. c) Quench at 5 °C with $\phi_0 = 0.148$. d) Quench at 10 °C with $\phi_0 = 0.111$.

can be calculated by using integral equation theory for simple liquids with a Percus–Yevick closure relation for a model of polydisperse spheres based on the algorithm in ref. 32. The square well potential is given by

$$U_{SW}(r) = \begin{cases} \infty & 0 < r < 2a_{eff} \\ -\varepsilon & 2a_{eff} < r < 2a_{eff}(1+\lambda) \\ 0 & r > 2a_{eff}(1+\lambda) \end{cases}$$

where $a_{eff}$ is an effective hard sphere radius, and $\varepsilon$ and $\lambda$ are the depth and the range of the square well, respectively. While square well potentials have unphysical shapes, they have been widely used to successfully model colloids with short range attractions since the relevant physical properties were found to depend only weakly on the shape of the potential.[33]

The parameters were taken from a fit of SANS data obtained with a temperature and a concentration series in the fluid state above the coexistence curve. Typical results are shown in Fig. 5a. We obtain a satisfying fit of the temperature dependence of the structure factor with a square well interparticle interaction. For the concentration series at a given temperature the range and the depth of the well could be maintained constant, with $\varepsilon/kT = -3.52$ for 20 °C and $-3.24$ for 30 °C and $\lambda = 2.2\%$ (data not shown). The study of the structure factor as a function of temperature then yields a direct relation between the depth of the short range attraction, $\varepsilon$ and $T$. For a given concentration, $\phi = 0.052$, $S(q)$ could be fitted maintaining the range of the attraction constant ($\lambda = 2.2\%$) as shown in Fig. 5a. This is consistent with the presence of an isosbestic point at $q \approx 0.8$ nm$^{-1}$. Isosbestic points indeed appear in scattering experiments when adjusting the strength of attraction at constant range.[34–36] The analysis of the data shown in Fig. 5a provides an estimate of the temperature dependence of $\varepsilon$ as shown in Fig. 5b. $\varepsilon/kT$ scales linearly with temperature, which would suggest that the main temperature dependence of the interparticle interaction is simply through the temperature factor $kT$, while other specific temperature effects, such as changes in the hydration of lysozyme, if present, play a minor role. Note, however, that while a simple square well potential as used here is capable of reproducing the structure factors at all temperatures, it fails when simultaneously trying to quantitatively predict the corresponding virial coefficients $B_2$ as a function of $T$. In this case it is necessary to depart from a purely centrosymmetric potential and include a certain degree of patchiness, at the same strength of the attraction.[31]

Having fixed the potential values for all relevant temperatures from an extrapolation of the data shown in Fig. 5b, we can next calculate the full effective structure factor that describes the local structure in samples with an arrested spinodal decomposition. Here we have to include contributions from the gas-like phase, given by an effective structure factor $S_1(q)$, and from the dense phase, given by $S_2(q)$, respectively. Assuming that the contribution of the gas phase (1) and the glass phase (2) are uncorrelated, the resulting structure factor $S(q,\phi_0,T_f)$ of a sample with initial concentration $\phi_0$ and final temperature $T_f$ is given by

$$S_{cal}\left(q, \phi_0, T_f\right) = \left[\frac{(1-h)\phi_1}{\phi_0} S_1(q, \phi_1, \varepsilon) + \frac{h\phi_2}{\phi_0} S_2(q, \phi_2, \varepsilon)\right] \tag{4}$$
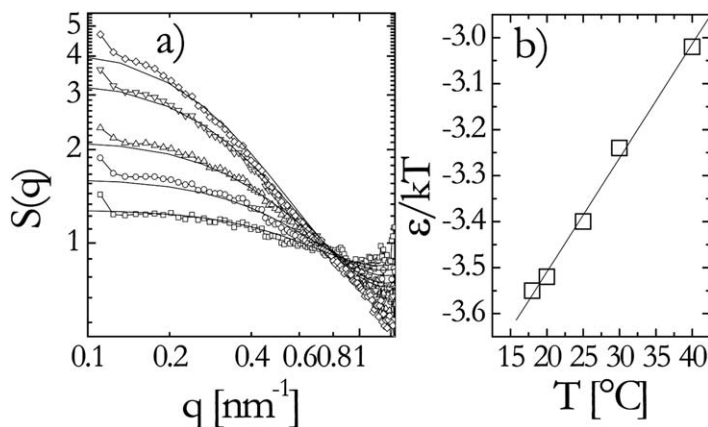


**Fig. 5** a) $S(q)$ from SANS for different temperatures (from below: 18, 20, 25, 30, 40 °C) at $\phi = 0.052$. $S(q \rightarrow 0)$ increases monotonously as temperature decreases. The lines show the calculated $S(q)$. b) Evolution of $\varepsilon$ obtained from the fit of $S(q)$ in a) as a function of temperature.

This journal is © The Royal Society of Chemistry 2012

where all parameters have been determined independently from centrifugation experiments (Tab. 1) and SANS measurements in the liquid phase above the binodal (Fig. 5). This approach is motivated by the fact that in general repulsive and attractive glasses show typical fluid structure as the system goes through the dynamical arrest transition. The results of these calculations are shown in Fig. 4. Although this empirical model provides surprisingly good agreement at intermediate and high $q$, deviations at lower values of $q$ show that the approach does not capture the structure on larger length scales. Therefore we extend our analysis to computer simulations using a reverse Monte Carlo method.

### 3.4 Russian doll reverse Monte Carlo analysis of the intensity

So far we have been able to show that we obtain quantitative and consistent information about the structure of the arrested spinodal from a combination of scattering and optical microscopy over a very large range of length scales. A remaining difficulty is the structure at intermediate length scales or wave vectors, in particular if we like to get information beyond the fact that the extended Porod region indicates the formation of well separated regions having different concentrations and a well defined interface. Therefore, we have developed a new reverse Monte Carlo (RMC) method for the analysis of the structure of the concentrated phase based on the scattering data (Fig.6).

The use of standard direct Monte Carlo would be extremely time consuming, as typically some $10^6$ particles make up the biggest structures. Indeed, the experimental $q$-range is very large (down to 0.01 nm$^{-1}$), and the size of the primary lysozyme monomer quite small ($a = 1.6$ nm). To limit the computational effort, we need a course graining procedure, which we term 'Russian Doll RMC'. The idea is to describe the structure on a small length scale with few particles, regroup them into a '*meta*-particle', and use it to build a higher order structure, and so on. Each level is described by an ensemble of particles, using a conventional Reverse Monte Carlo (RMC) algorithm.[37,38] The idea is to build a first-guess-structure, and improve the agreement of its $I(q)$ in the corresponding $q$-range with the experimentally
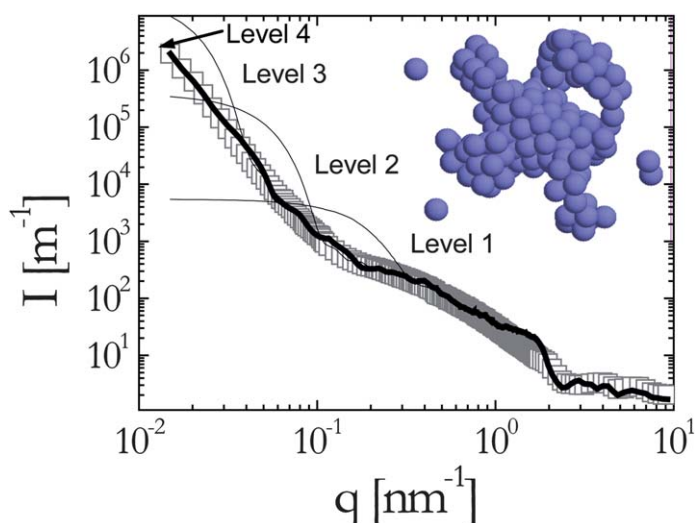


**Fig. 6** Intensity scattered by a sample after an arrested spinodal decomposition (□). The thin lines show the intensity scattered by the *meta*-particles at different levels. The thick line shows the result of the simulation. The Inset shows an example of the simulation results in real space where aggregation of third level metaparticles (radius 131 nm) are shown.

measured one by randomly displacing individual subunits. These displacements are confined inside the spherical next-order metaparticles, which is a way to control internal volume fraction and interactions. Due to possible interpenetration of the less dense metaparticles, the excluded volume condition is maintained only on the smallest length scale. Structure factors can then be calculated using the Debye formula.[39] Intensities are obtained by straightforward multiplication of lysozyme form factor and structure factors for (on average) spherically symmetric metaparticles, followed by the addition of the dilute-phase intensity.

We focus on the temperature quench to 13 °C ($\phi_0 = 0.148$), but a very similar approach could be applied to the other samples. In Fig. 6, the experimental intensity is compared to the successive fits on the various length scales. At the smallest scale, 50 lysozyme particles make up a first metaparticle of radius $a_{m1} = 11.5$ nm. Some deviations can be observed, presumably due to non sphericity of the proteins. At intermediate $q$, 70 of these metaparticles form the next higher structure of radius $a_{m2} = 44.0$ nm, 50 of which are then regrouped on the third level ($a_{m3} = 131.0$ nm), and finally 200 of these biggest particles make up the largest structure (overall size 1000.0 nm). This structure represents $3.5 \times 10^6$ lysozyme particles which make up the dense phase (volume fraction $\phi_2 = 0.35$) inside the dilute one. For illustration, this biggest structure is plotted as an inset in Fig. 6. It seems to reproduce a microscopic phase separation, the typical length scale of which—two to three metaparticle diameters—approaches one micron (consistent with light scattering and microscopy). The scattered intensity is found to be well fitted by the RMC simulation. In particular, all major features (low-$q$ Porod regime, break in slope, high-$q$ lysozyme structure) are reproduced in an at least semi-quantitative manner, and the resulting local volume fraction of the dense phase $\phi_2 = 0.35$ is in very good agreement with the value $\phi_2 = 0.34$ obtained from the centrifugation experiments (Tab. 1). The Russian-Doll RMC method presented here has been tested on simulated aggregate structures with two levels, and the results are given in the appendix. It is however clear that for future work, the limits of this approach will need to be tested, and in particular the set of working parameters (size and number of metaparticles) will have to be determined.

## 3.5 Mechanical properties

Having established that the arrested spinodal decomposition in lysozyme solutions results in the formation of a bicontinuous network with a coexisting dilute fluid phase and an arrested glassy high density backbone with a density and correlation length that decreases with increasing quench depth, we next investigated the resulting mechanical properties of these samples. Typical results from such a series of different quench depths $T_f$ at constant initial volume fraction $\phi_0 = 0.111$ are shown in Fig. 7a. Shown are data from creep tests as the time dependence of the inverse creep compliance $J^{-1}(t)$. The creep measurements reveal an unusual mechanical response with two plateaus at short and long times, respectively, separated by a dissipative regime at intermediate times. These plateaus can be associated with the short ($G_\infty$) and long ($G_0$) time elastic moduli that have already previously been found in oscillatory shear and creep measurements that underwent an arrested spinodal.[11] We do in fact find in all of the arrested samples two elastic plateaus at high ($G_\infty$) and low ($G_0$) frequencies or short and long times, with $G_\infty \gg G_0$, and the results from the creep measurements and the oscillatory shear measurements are all fully consistent.

Fig. 7b summarizes the resulting values of the moduli $G_\infty$ and $G_0$ for the series of different quench depths $T_f$ at a constant initial concentration $\phi_0 = 0.111$. We see that while the high frequency modulus $G_\infty$ appears to be independent of $T$, the low frequency modulus $G_0$ dramatically increases with decreasing temperature over almost 3 orders of magnitude for the range of $T$ investigated. The two moduli appear to merge close to the extrapolated position of the arrest line for $\phi_0 = 0.111$, *i.e.* at
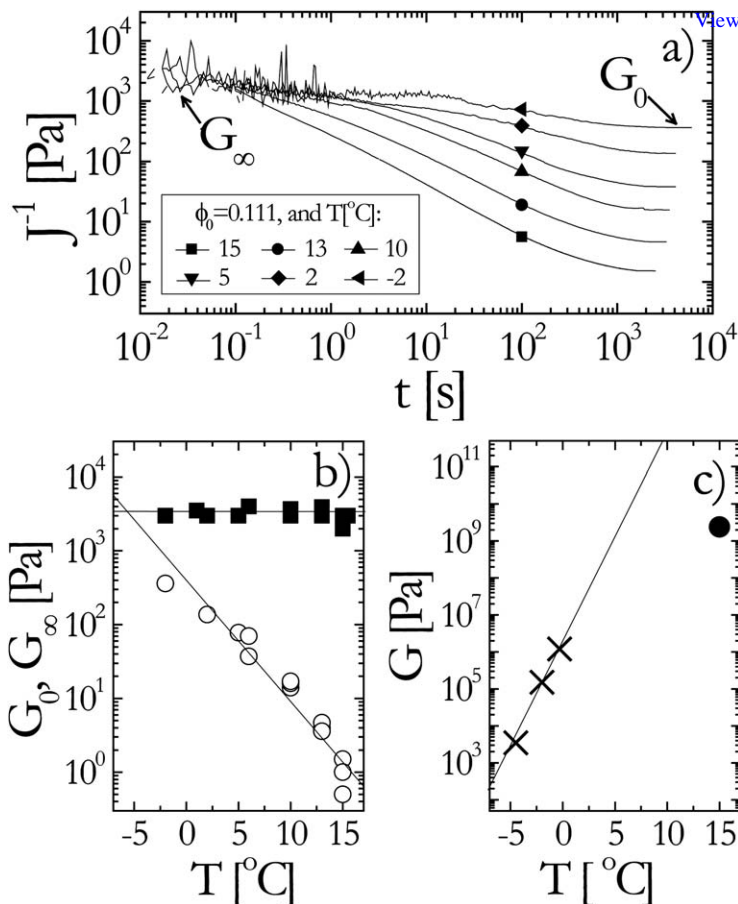
**Fig. 7** a) Results from creep experiments showing the time evolution of the compliance $J^{-1}$ in the linear regime at $\phi = 0.111$ for a series of different temperature quenches to $T_f = 15\,°C$ ($\blacksquare$), $13\,°C$ ($\bullet$), $10\,°C$ ($\blacktriangle$), $5\,°C$ ($\blacktriangledown$), $2\,°C$ ($\blacklozenge$), $-2\,°C$ ($\blacktriangleleft$). The line shows the conversion of the corresponding compliance $J^{-1}$ into storage and loss moduli. b) Dependence of $G_\infty$ ($\blacksquare$) and $G_0$ ($\circ$) on $T_f$ for $\phi_0 = 0.111$. c) Intersection points of $G_\infty$ and $G_0$ from the $T$-dependence for three different initial concentrations $\phi_0 = 0.111, 0.148, 0.186$ (x). Also shown is the theoretical estimate of the modulus of an attractive glass at the intersection point of the arrest tie line and the binodal ($\bullet$, see text for details).

$T_g(\phi_0) = -5\,°C$. Given the fact that the mechanical response of the samples with two elastic moduli most likely reflects the bicontinuous structure with a coexistence of a dilute liquid and a dense solid-like phase,[11] such a coincidence of the intersection point of $G_\infty(\phi)$ and $G_0(\phi)$ with the position of the arrest line is not unexpected. We do in fact expect that for a quench to the arrest line or below, *i.e.* within region III of the state diagram in Fig. 2a, the sample is in a homogeneous attractive glass state. Here a bicontinuous texture should no longer exist as the spinodal decomposition process becomes immediately arrested upon a quench to $T_f \leq T_g$. Therefore, we should then also find a single modulus $G = G_\infty = G_0$ only. Indeed we find the same behavior for all temperature series at different initial volume fractions investigated, with the intersection points located on the extrapolated arrest line in Fig. 2a.

The resulting values of the moduli at the different intersection points are shown in Fig. 7c. These values reflect the mechanical properties of the attractive glasses at different positions on the arrest line in Fig. 2a. They indicate that an arrested

spinodal decomposition indeed allows us to create soft solids with mechanical properties that may vary over many orders of magnitude. While we have so far only covered the low temperature/volume fraction part of the arrest line dividing regions II and III in Fig. 2a, we can at least estimate the maximum attainable value for G that would correspond to the intersection of the arrest line and the binodal, *i.e.* at a value of $\phi_0 \approx 0.35$ and $T \approx 15\,°C$. Under these conditions, a prediction for attractive glasses formed by colloids with short range attractions should provide at least some guidelines. We can use a simple model for the modulus of an attractive glass $G_{ag}$ given by $G_{ag} \approx U_a/(r_{loc}^2 \sigma)$, where $U_a$ is the value of the potential at contact, *i.e.* $U_a = U(r = \sigma)$, and $r_{loc}$ is the localization length of the particles trapped in the attractive well.[40,41] If we use $U_a \approx 3kT$ and $r_{loc} = \lambda a$, with $\lambda = 2.22\%$ the range of the attraction, we obtain a value of $G_{ag} \approx 2.4 \times 10^9$ Pa. While we have not explored a sufficiently large range of concentrations and temperatures yet, Fig. 7c nevertheless already indicates that an arrested spinodal decomposition for attractive proteins or food colloids could be a very interesting mechanism for forming gels with tunable properties.

## 4 Conclusions—lessons learned for making food gels

Our combined SANS, SAXS and rheology experiments have confirmed that quenching aqueous lysozyme solutions at sufficiently low temperatures below the binodal leads to an arrested spinodal decomposition and the formation of a bicontinuous structure with a dilute fluid gas-like phase and a dense glass-like solid backbone. The formation of a well defined interface and values of the local concentration of the dense phase in agreement with those previously obtained through ex-situ centrifugation experiments further support these previous studies. When combining the findings in Fig. 7b and 3a, we realize that we can create solid-like protein samples whose structural and mechanical properties can be varied and tailored over an extremely large range in a very controlled way through an arrested spinodal decomposition process. While in particular the origin of the dependence of the mechanical properties on quench depth and concentration is not well understood currently, it seems ultimately connected to the particular bicontinuous structure of the arrested spinodal network created by the interplay between the early stage of a spinodal decomposition and the position of the glass line. This obviously opens up new routes to prepare gel-like systems with adjustable structural and mechanical properties in materials and food science. If this is a generic behavior of colloids with short range attractions as postulated also in Fig.1, we can then try to use for example a depletion interaction caused by the addition of small non-adsorbing polymers to suspensions of food colloids such as casein micelles or emulsion droplets in order to create food gels with tunable structural and mechanical properties through a very simple mixing process.

We tested the feasibility of such an approach using casein micelle suspensions with added PEO at a concentration $c_p$, where PEO induces an attractive depletion interaction. These first tests are indeed encouraging, we have qualitatively observed the same phase behavior as in lysozyme, with the existence of liquid states at low $c_p$ and a liquid–liquid phase separation at higher values of $c_p$ that then becomes arrested at sufficiently high polymer concentrations. Moreover, the arrested samples also exhibit a bicontinuous network structure, again qualitatively similar to those already observed for lysozyme solutions, as demonstrated in Fig. 8. The figure shows confocal laser scanning microscopy pictures from casein micelle suspensions at a constant volume fraction $\phi = 0.25$ with added PEO at two different polymer concentrations $c_p$, *i.e.* for different strengths of a short range depletion interaction, under conditions where phase separation is arrested. While PEO is of course not a food polymer, we use it as a simple and well defined model of a linear flexible and non-adsorbing polymer to create a well defined depletion interaction between the casein micelles. Given the casein radius of $a_{casein} \approx 100$ nm and the radius of
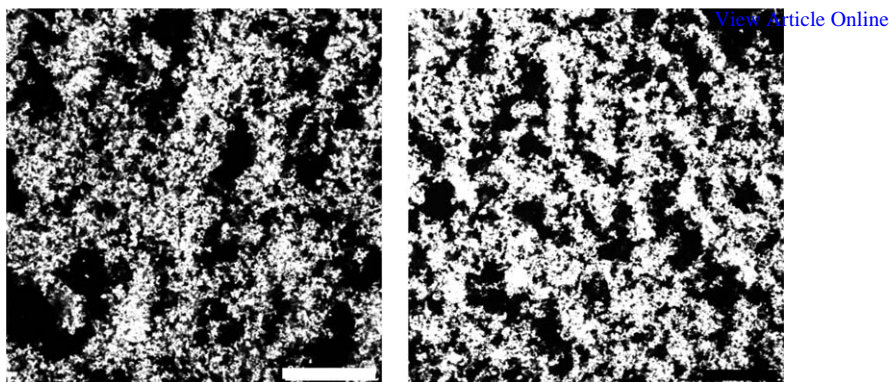
**Fig. 8** Confocal images in the XY plane of arrested casein–PEO mixtures. The casein phase is stained with Rhodamine B and is shown in white. The images show suspensions with a casein volume fraction $\phi = 0.25$ and two polymer concentrations $c_p = 10$ mg mL$^{-1}$ (left) and 12 mg mL$^{-1}$ (right). Scale bars denote 50 μm.

gyration of PEO of $R_g \approx 16$ nm in the dilute limit, the range of the resulting depletion interaction is less than 15% of the particle radius, *i.e.* sufficiently short ranged to result in a metastable liquid–liquid phase separation scenario. For a sufficiently strong depletion attraction we indeed find arrested spinodal decomposition resulting in solid-like samples with a bicontinuous network structure such as the ones shown in Fig. 8, with a mesh size that depends on the quench depth (polymer concentration) similar to what has been observed previously for lysozyme (Fig. 3a).

We are currently performing a systematic investigation of the phase diagram and the resulting structural and mechanical properties with a particular focus on samples that underwent an arrested spinodal decomposition. It is clear that further experimental and theoretical input and more refined computer simulations will be needed in the future in order to achieve a quantitative understanding of the interplay between the local and global network structure and the resulting intricate mechanical response. However, given the enormously large range of length scales involved in these systems this will not be an easy task. Finally, one should also take into account the added possibilities that the presence of an additional Coulomb repulsion provides as shown schematically in Fig. 1. The results discussed in this paper do however clearly demonstrate the existence of a variety of mechanisms that can produce dynamically arrested states with solid-like appearance for colloids with short range attractions, mechanisms that should be possible to exploit in suspensions of food colloids through controlled application of a non-adsorbing food polymer.

# Appendix

## A.1 One-level reverse Monte Carlo

The aim of our implementation of the standard RMC algorithm with simulated annealing is to find a family of real-space configurations of spherical beads the scattering function of which is consistent with the experimentally observed one. In this appendix, the method is tested with model aggregates. First, an aggregate is generated, and its bead-bead structure factor $S(q)$ is calculated. Then, this structure factor is used as an input to the standard aggregate RMC algorithm for aggregates as presented in ref. 37. Note that the topology of the aggregate is conserved, in the sense that beads must always touch, and the aggregate always remains a single connected assembly of beads. The outcome is a series of real-space snapshots of aggregates, which can be compared in shape and size to the original aggregate (known by

construction in this test). Naturally, the question of how to quantify good agreement arises. A close or even identical pair correlation function is fulfilled if the RMC-fit of $S(q)$ is good. Therefore, the radius of gyration of the resulting aggregate, as well as the local coordination numbers and intermediate scaling regimes (if present), are trustworthy. Here, we limit ourselves to a presentation of snapshots which show the overall robustness of the method.

In Fig. 9, the structure factor of the aggregate shown in the upper inset is compared to the final RMC-fit, and perfect agreement is found. The original aggregate was constructed by an individual diffusion process of sticky beads (bead radius 5 nm, 100 beads). Its structure factor reflects the 3D-arrangement, starting with the total aggregation number at $q \to 0$, the radius of gyration in the Guinier regime, and the internal structure with strong correlation peaks due to the excluded volume of monodisperse beads. A possible compatible 3D-arrangement found by the RMC-algorithm is depicted in the lower inset. Visual comparison with the original one shows that the algorithm produces a trustworthy configuration. Needless to say, the result is not unique: small changes obtained by displacing one bead will not affect the $S(q)$, as long as they do not induce notable changes in the local coordination or overall shape of the aggregate.

## A.2 Two-level RD-RMC

A two-level RD-RMC was applied to a bigger aggregate (bead radius 5 nm, 1000 beads), following the same concept as in the previous section. Note that the generalization to higher level aggregates as shown in this article is straightforward. The aggregate structure factor has been constructed using the same algorithm as previously. It is shown in Fig. 10, with the 3D-representation of the original aggregate in the upper inset on the right.

This calculated structure factor is again the input of the RMC algorithm. We have chosen a first level of 30 beads. The standard one-level RMC-algorithm as in Fig. 10 was applied to the structure factor of the 1000-bead aggregate, in the high-$q$ range
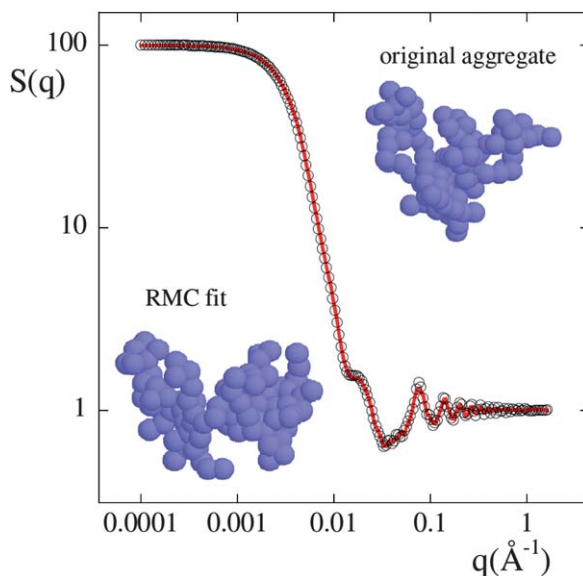


**Fig. 9** Standard RMC analysis of the structure factor of a known aggregate (symbols) of 100 beads. The RMC-fit is the solid line. Upper inset: original aggregate configuration. Lower inset: RMC-snapshot compatible with $S(q)$.
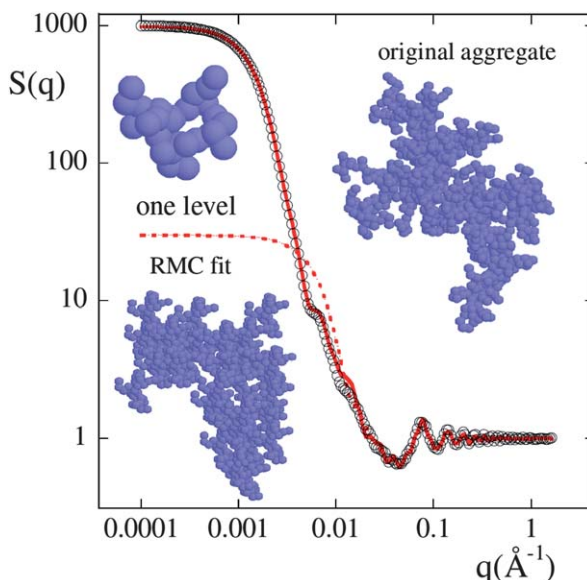
**Fig. 10** Two-level RD-RMC analysis of a known aggregate of 1000 beads. The one-level (30 beads, dotted line) and two-level (33 first level aggregates, solid line) RMC-fits are compared to the total structure factor (black circles). In the upper inset on the right, the initial aggregate, on the left the first level one, and below the total one made of combinations of level one and two are shown.

$(q > 0.01 \mathring{A}^{-1})$. The agreement between the dotted curve and the structure factor is seen to be good in this $q$-range. The first level aggregate of 30 beads (shown in the upper left inset) was then used as an input for the two-level fit, of 33 aggregates. The result, now over the complete $q$-range, is equally satisfactory. In the lower inset, the reconstruction of the complete aggregate from level one and two is shown. It compares reasonably well with the original aggregate, shown in the top right inset.

## Acknowledgements

## References

1 R. Mezzenga, P. Schurtenberger, A. Burbidge and M. Michel, *Nat. Mat.*, 2005, **4**, 729.
2 E. Zaccarelli, *J. Phys.: Condens. Matter*, 2007, **19**, 323101.
3 K. A. Dawson, *Curr. Opin. Colloid Interface Sci.*, 2002, **7**, 218.
4 F. Sciortino, *et al.*, *Comput. Phys. Commun.*, 2005, **169**, 166.
5 W. C. K. Poon, *et al.*, *Faraday Discuss.*, 1995, **101**, 65.
6 F. Cardinaux, E. Zaccarelli, A. Stradner, S. Bucciarelli, B. Farago, S. Egelhaaf, F. Sciortino and P. Schurtenberger, *J. Phys. Chem. B*, 2011, **115**, 7227.

7  P. Pusey and W. van Megen, *Nature*, 1986, **320**, 340–342.
8  K. N. Pham, *et al.*, *Science*, 2002, **296**, 104.
9  V. Trappe and P. Sandkuhler, *Curr. Opin. Colloid Interface Sci.*, 2005, **18**, 494500.
10  S. Romer, F. Scheffold and P. Schurtenberger, *Phys. Rev. Lett.*, 2000, **85**, 4980.
11  F. Cardinaux, T. Gibaud, A. Stradner and P. Schurtenberger, *Phys. Rev. Lett.*, 2007, **99**, 118301.
12  E. B. Sirota, H. D. Ou-Yang, S. K. Sinha, P. M. Chaikin, J. D. Axe and Y. Fujii, *Phys. Rev. Lett.*, 1989, **62**, 1524.
13  P. Wette, *et al.*, *J. Chem. Phys.*, 2010, **132**, 131102.
14  A. Stradner, H. Sedgwick, F. Cardinaux, W. C. K. Poon, S. U. Egelhaaf and P. Schurtenberger, *Nature*, 2004, **432**, 492.
15  A. I. Campbell, V. J. Anderson, J. van Duijneveldt and P. Bartlett, *Phys. Rev. Lett.*, 2005, **94**, 208301.
16  H. Sedgwick, A. Kroy, K., Salonen, M. B. Robertson, S. U. Egelhaaf and W. C. K. Poon, *Eur. Phys. J. E*, 2005, **16**, 77–80.
17  C. J. Dibble, M. Kogan and M. J. Solomon, *Phys. Rev. E*, 2006, **74**, 041403.
18  V. Gopalakrishnan and C. F. Zukoski, *Phys. Rev. E*, 2007, **75**, 021406.
19  A. Shalkevich, A. Stradner, S. K. Bhat, F. Muller and P. Schurtenberger, *Langmuir*, 2007, **23**, 3570–3580.
20  F. Zhang, M. W. A. Skoda, R. M. J. Jacobs, R. A. Martin, C. M. Martin and F. Schreiber, *J. Phys. Chem. B*, 2007, **111**, 251–259.
21  W. Pan, O. Galkin, L. Filobelo, R. L. Nagel and P. G. Vekilov, *Biophys. J.*, 2007, **92**, 267–277.
22  O. Gliko, W. Pan, P. Katsonis, N. Neumaier, O. Galkin, S. Weinkauf and P. G. Vekilov, *J. Phys. Chem. B*, 2007, **111**, 3106–3114.
23  S. Boutet and I. K. Robinson, *Phys. Rev. E*, 2007, **75**, 021913.
24  N. Destainville, *Phys. Rev. E*, 2008, **77**, 011905.
25  N. Javid, K. Vogtt, C. Krywka, M. Tolan and R. Winter, *Phys. Rev. Lett.*, 2007, **99**, 028101.
26  L. Ianeselli, F. Zhang, M. W. A. Skoda, R. M. J. Jacobs, R. A. Martin, S. Callow, S. Prevost and F. Schreiber, *J. Phys. Chem. B*, 2010, **114**, 3776–3783.
27  T. Gibaud and P. Schurtenberger, *J. Phys.: Condens. Matter*, 2009, **21**, 322201.
28  P. J. Lu, E. Zaccarelli, F. Ciulla, A. B. Schofield, F. Sciortino and D. A. Weitz, *Nature*, 2008, **453**, 499.
29  T. Gibaud, F. Cardinaux, J. Bergenholtz, A. Stradner and P. Schurtenberger, *Soft Matter*, 2011, **7**, 857.
30  J. S. Pedersen, *J. Appl. Cryst.*, 2004, **37**, 369.
31  C. Gogelein, G. Nagele, R. Tuinier, T. Gibaud, A. Stradner and P. Schurtenberger, *J. Chem. Phys.*, 2008, **129**, 085102.
32  R. Klein and B. D'Aguanno, *Light Scattering, Principles and Development*, Oxford, 1996.
33  M. G. Noro and D. Frenkel, *J. Chem. Phys.*, 2000, **113**, 2941–2944.
34  M. H. G. Duits, R. P. May, A. Vrij and C. G. D. Kruif, *Langmuir*, 1991, **7**, 62.
35  X. Ye, T. Narayanan, P. Tong and J. S. Huang, *Phys. Rev. Lett.*, 1996, **76**, 4640.
36  E. Dubois, V. Cabuil, F. Boue and R. Perzynski, *J. Chem. Phys.*, 1999, **111**, 7147.
37  J. Oberdisse, P. Hine and W. Pyckhout-Hintzen, *Soft Matter*, 2007, **2**, 476.
38  R. McGreevy, *J. Phys.: Condens. Matter*, 2001, **13**, 877.
39  P. Debye, *Phys. Coll. Chem.*, 1947, **51**, 18.
40  S. A. Shah, Y. L. Chen, K. S. Schweizer and C. F. Zukoski, *J. Chem. Phys.*, 2003, **119**, 8747.
41  M. E. Cates, M. Fuchs, K. Kroy, W. C. K. Poon and A. M. Puertas, *J. Phys.: Condens. Matter*, 2004, **16**, S4861.

This journal is © The Royal Society of Chemistry 2012